

A gate tunable transmon qubit in planar Ge

Oliver Sagi,^{1,*} Alessandro Crippa,² Marco Valentini,¹ Marian Janik,¹ Levon Baghumyan,¹ Giorgio Fabris,¹ Lucky Kapoor,¹ Farid Hassani,¹ Johannes Fink,¹ Stefano Calcaterra,³ Daniel Chrastina,³ Giovanni Isella,³ and Georgios Katsaros¹

¹*Institute of Science and Technology Austria, Am Campus 1, 3400 Klosterneuburg, Austria*

²*NEST, Istituto Nanoscienze-CNR and Scuola Normale Superiore, I-56127 Pisa, Italy*

³*L-NESS, Physics Department, Politecnico di Milano, via Anzani 42, 22100, Como, Italy*

(Dated: March 26, 2024)

Gate-tunable transmons (gatemons) employing semiconductor Josephson junctions have recently emerged as building blocks for hybrid quantum circuits. In this study, we present a gatemon fabricated in planar Germanium. We induce superconductivity in a two-dimensional hole gas by evaporating aluminum atop a thin spacer, which separates the superconductor from the Ge quantum well. The Josephson junction is then integrated into an Xmon circuit and capacitively coupled to a transmission line resonator. We showcase the qubit tunability in a broad frequency range with resonator and two-tone spectroscopy. Time-domain characterizations reveal energy relaxation and coherence times up to 75 ns. Our results, combined with the recent advances in the spin qubit field, pave the way towards novel hybrid and protected qubits in a group IV, CMOS-compatible material.

INTRODUCTION

Hybrid quantum circuits interface different physical paradigms in the same platform, leading to devices with novel functionalities [1, 2]. Specifically, hybrid qubits combining superconductors and semiconductors merge the maturity of superconducting quantum circuits with the inherent tunability of semiconductors. Gate-tunable transmons (gatemons) [3–5], parity-protected qubits [6], and Andreev spin qubits (ASQs) [7, 8] are representative examples of recent achievements. In the development of hybrid qubits on novel material platforms, demonstrating coherent interaction between a microwave resonator and a Josephson junction is a paramount step. Experimentally, the most direct approach to achieve this interaction is through capacitive coupling between a resonator and a gatemon circuit [9–12]. This coupling enables dispersive readout [13] and, when combined with coherent control, serves as the foundation for progressing towards advanced hybrid circuits.

A prominent example is ASQs, which combine the advantages of both superconducting and semiconductor spin qubit platforms [7, 8, 14–16]. Semiconductor spin qubits offer low footprint and high anharmonicity, but implementing long-range coupling over many qubits remains challenging, though remarkable advances have been recently demonstrated [17–19]. Superconducting transmon circuits provide well-mastered control and readout via microwave signals at the expense of large footprints and lower anharmonicity, posing challenges to scalability and fast operations. Finding a suitable platform to merge the two systems is a formidable task. It requires a low microwave-loss substrate (unless flip-chip technology is used [20]), transparent semiconductor-superconductor interfaces, and material free from nuclear spins for optimal spin qubit operation.

In the field of semiconductor spin qubits, Si is an attractive material choice as a result of the mature complementary metal-oxide-semiconductor (CMOS) technology [21] and isotopic purification [22]. Moreover, Si-based platforms have demonstrated the capability of hosting microwave resonators coupled to quantum dots [18, 19, 23–25]. However, the absence of Fermi level pinning makes it challenging to proximitize silicon without using doping or annealing techniques [26, 27]. III-V semiconductor compounds, on the other hand, have emerged as the natural solution for hybrid devices due to the high-quality epitaxial aluminum (Al) growth, yielding a hard gap (i.e. free of subgap states) and a transparent interface [28–31]. Nevertheless, the non-zero nuclear spin limits the spin qubit coherence to ~ 10 ns [32]. Ge, and in particular Ge/SiGe heterostructures, have shown great potential for highly-coherent spin qubits and gate-tunable hybrid Josephson junctions [33–40], thus allowing the integration of semiconducting qubits with superconducting qubits on the same substrate.

Ge gatemons within Ge/Si core/shell nanowires have been recently realized [41, 42]. However, while such CVD-grown core/shell wires have demonstrated ultrafast spin qubits [43, 44] they face challenges in terms of spin dephasing times and scale-up. To circumvent both issues, we build on the success of two-dimensional implementations in InAs/InGaAs heterostructures [5, 45] and realize a gatemon based on a Ge/SiGe heterostructure where superconductivity is induced into the Ge hole gas by proximity from an Al layer evaporated on top of the SiGe spacer. The gatemon resonant frequency is electrically tunable in a range of ~ 5 GHz and exhibits a quasimonotonic, linear dependence on the gate voltage. The qubit relaxation time T_1 spans from ~ 80 ns to ~ 20 ns by varying the gate voltage, while T_2^* does not show any clear trend. A control qubit on the same material stack

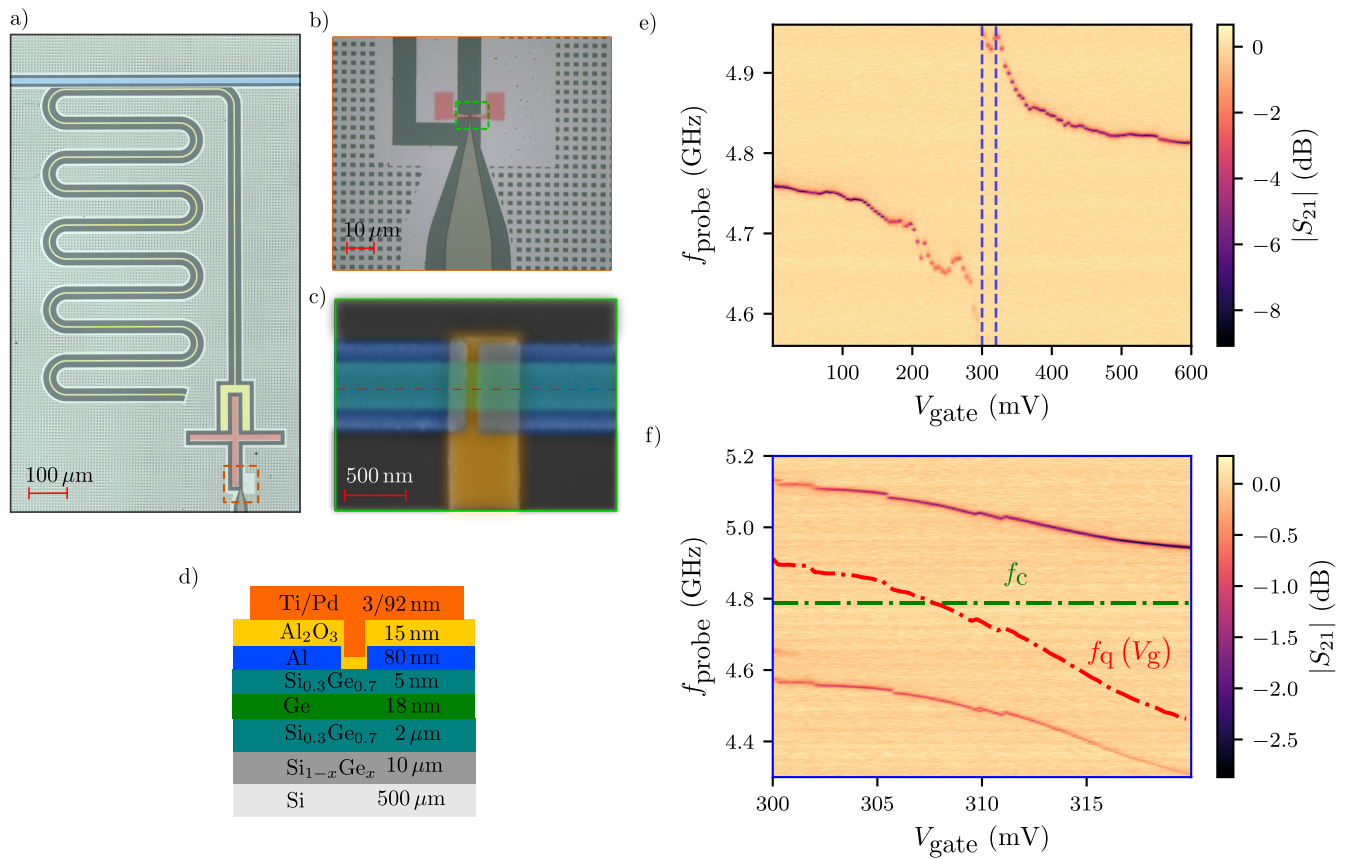


FIG. 1. Overview of the complete Ge gatemon device and resonator spectroscopy measured with a Vector Network Analyzer. a) Optical microscope image showcasing the entire device. A $\lambda/4$ notch-type coplanar waveguide resonator (yellow) is capacitively coupled to the cross-shaped qubit island (red) alongside a transmission line (blue) utilized for readout. The island is shunted to the ground through a gate-tunable semiconductor Josephson junction. b) Close-up view of the U-shaped mesa (highlighted in red). c) False-colored SEM image of the junction, depicting the junction where the evaporated aluminum (blue) extends over the mesa (light green) to proximitize the whole mesa. The gate line (orange) is intentionally extended on the right side to increase capacitance to the ground. d) Cross-section of the wafer stack along the red-dashed line in Fig. 1c. e) Gate-dependence of the normalized resonator transmission after background correction. f) Close-up view of the avoided crossing after background correction and boxcar averaging with a window size of 8 points. The dashed green line represents the bare resonator frequency, while the red dashed line indicates the qubit frequency extracted from the two peaks according to Eq. 2.

using a superconductor-insulator-superconductor (SIS) junction exhibits a T_1 about five times longer than the semiconductor junction, and T_2^* approaches $2T_1$. We discuss potential limitations in the Ge gatemon arising from the substrate and device layout.

DEVICE

An optical image of our device is shown in Fig. 1. We adopt a planar ‘Xmon’ geometry, known to maintain balance among coherence, connectivity, and swift control [46, 47]. The core of the device is the semiconductor junction defined on the U-shaped mesa (see Fig. 1b and c) with a width of ~ 450 nm and a junction length of ~ 150 nm. The critical current I_c through the semiconductor junction determines the Josephson energy

($E_J = \hbar I_c / 2e$, with \hbar the reduced Planck constant and e the electron charge), which sets the qubit frequency together with the charging energy E_c of the cross-shaped island. The island and the semiconductor junction together form the qubit circuit. The charging energy of the island is designed to be $E_c/h \sim 200$ MHz to set the qubit frequency to be compatible with the 2 – 10 GHz range of our electronics and to operate in the transmon regime $E_J \gg E_c$ [48]. The gatemon is coupled to a notch-type, $\lambda/4$ resonator with a loaded quality factor of $Q_1 \sim 1400$ (see Fig. 6b). The fabrication process flow is detailed in the Methods Section.

RESONATOR SPECTROSCOPY

We investigate the gate tunable qubit-resonator interaction by monitoring the feedline scattering parameter S_{21} . The microwave power is kept low enough such that the average photon population of the resonator is approximately 1. By applying a voltage V_g on the Ti/Pd gate, we modify the critical current of the junction, which turns into a modulation of the qubit frequency: $f_q \propto \sqrt{I_c(V_g)}$. As displayed in Fig. 1e, the qubit exhibits one pronounced avoided crossing with the resonator. When the qubit is in resonance with the resonator, we observe two peaks in $|S_{21}|$ (at frequency f_+ and f_- , see Fig. 1f), a hallmark of two hybridized qubit-resonator states due to the strong coupling regime. To extract the coupling strength g we fit the splitting: $\delta = f_+ - f_-$ according to the following equation [4]:

$$\delta = \sqrt{(f_q - f_c)^2 + 4(g/2\pi)^2}, \quad (1)$$

as illustrated in Fig. 6c, where f_q and f_c are the bare qubit and resonator frequencies respectively. The fit yields $g/2\pi \approx 270$ MHz, consistent with electrostatic simulations. We also extract the qubit frequency:

$$f_q = (f_+ + f_-) - f_c, \quad (2)$$

shown with a red dashed line in Fig. 1f. We obtain the bare resonator frequency from an independent high-power resonator spectroscopy measurement. We note that, in contrast to nanowire gatemons [6, 49], we observe only one avoided crossing (refer to Fig. 6 for a broader gate voltage range), suggesting a smooth and monotonic (albeit still suffering from discrete charge jumps) frequency dispersion. In Fig. 8, we present additional resonator spectroscopy on a separate device with ~ 50 nm shorter channel length exhibiting similar behaviour.

QUBIT SPECTROSCOPY

We now investigate the qubit frequency dependence in a broader gate voltage range than Fig. 1f. To do that, we move the qubit to the dispersive regime ($|\Delta| = |f_q - f_r| > g/2\pi$) to probe the qubit eigenstates. We adopt a conventional two-tone spectroscopy technique by applying a $2 \mu\text{s}$ long drive tone on the gate line followed by a 150 ns readout pulse on the resonator line. When the qubit drive matches f_q , we observe a peak in the resonator phase response. We choose the measurement frequency at each gate voltage to obtain all information in the phase of the measured signal. The observed peaks in Fig. 2a and b shift consistently with gate voltage; therefore, we attribute it to the qubit mode. The critical current and, thus, the qubit frequency increases with decreasing gate voltage since the charge

carriers are holes. In Fig. 2b, a second, faint line appears, corresponding to the $|1\rangle \rightarrow |2\rangle$ transition, which is a signature of a residual thermal population of the excited state. We do not observe this transition when the qubit is above the resonator. Similarly to the resonator spectroscopy, we see a monotonic gate voltage dependence of the qubit frequency interrupted by discontinuities at specific gate voltages, which we attribute to charge jumps. Below $V_g < 100$ mV the qubit enters an unstable regime, exhibiting two peaks in two-tone spectroscopy likely due to a two-level fluctuator interacting directly with the qubit [50]. Therefore, we disregard the data at $V_g < 100$ mV in the following analysis.

The qubit frequency can be tuned over a range spanning a few GHz, as shown in Fig. 2c. The junction is tunable even in a broader range, but the diminished readout visibility did not allow us to probe the qubit outside the $2 - 7$ GHz range. The grey-shaded areas in Fig. 2 panels c and d indicate the strong coupling regime discussed in Fig. 1f and parts of the dispersive regime where two-tone spectroscopy is not possible because of the reduced readout visibility.

We extract the anharmonicity at each gate voltage with a separate measurement by using three tones. A fixed frequency tone saturates the $|0\rangle \rightarrow |1\rangle$ transition while the frequency of a second tone is swept. We plot the measurement data in Fig. 10, while in Fig. 2d, we summarize the extracted anharmonicities at all measured gate voltages. All measured anharmonicities are lower than $-E_c \approx -200$ MHz, a signature of non-sinusoidal current-phase relation [51], varying from -180 to -60 MHz. The variation in anharmonicity illustrates how the gate voltage influences transparency [52], with increased transparency resulting in lower anharmonicity, as seen in Fig. 2d. While reduced anharmonicity indicates a good interface quality between the proximitized Ge and the Ge forming the weak link, it also hinders fast qubit operations. In the case of a short, ballistic junction, a fourfold decrease in anharmonicity is expected compared to an SIS junction as the transparency reaches one [52]. Our device shows an approximately threefold decrease accompanied by pronounced fluctuations around certain gate voltage values. In Fig. 9, a similar device with the same width but with a ≈ 50 nm shorter junction shows almost monotonic gate voltage dependence; the origin of this difference calls for further investigations.

COHERENT CONTROL

Next, we show coherent manipulation of the gatemon states. At a fixed gate voltage, we demonstrate X - Y rotations by applying a cosine-shaped drive pulse (indicated blue in Fig. 3a) followed by a readout pulse on the resonator line. We dynamically vary the amplitude and the duration of the drive pulse at each sequence. The plot

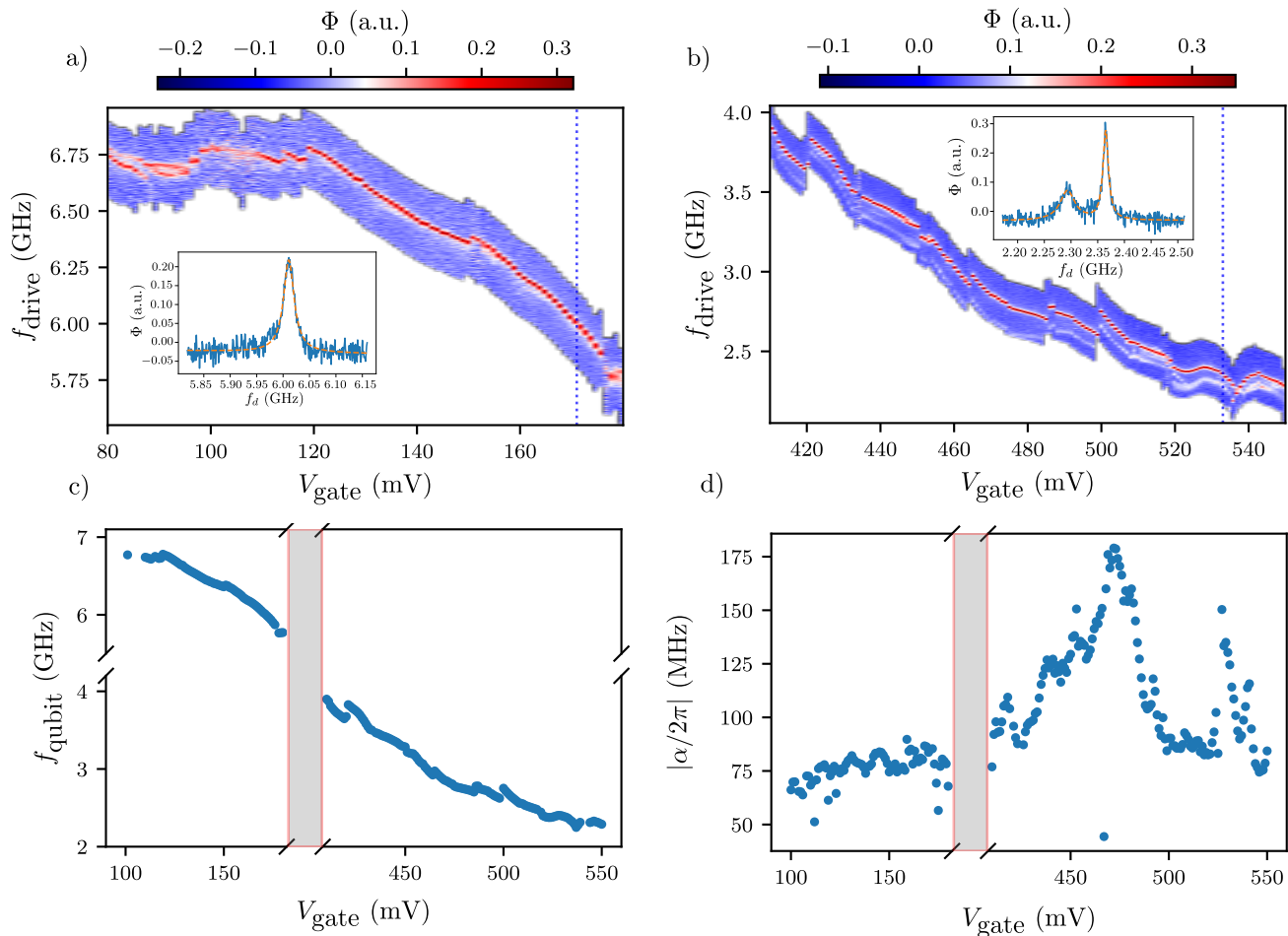


FIG. 2. Pulsed qubit spectroscopy. a)-b) Two-tone spectroscopy data after subtracting the average of each column and normalizing the trace. In panel a) (b), the qubit frequency is set above (below) the resonator frequency. We measure the transmitted signal phase after a $2 \mu\text{s}$ excitation. In b), we observe the $|1\rangle \rightarrow |2\rangle$ due to a residual excited state population. The insets show a linecut at $V_g = 171$ mV and $V_g = 533$ mV, respectively, along the blue dashed lines. The x and y axes correspond to f_{drive} and phase, respectively. c) Extracted qubit frequency from a) and b). We fit each trace with a Lorentzian (a pair of Lorentzian in the case of panel b), and the center yields the qubit frequency. d) Extracted anharmonicity from three-tone spectroscopy as explained in the main text. The anharmonicity is reduced compared to $-E_c$, indicating a non-sinusoidal current-phase relation.

in Fig. 3a shows a typical Rabi pattern, featuring oscillations with an increasing frequency as the drive amplitude increases. Notably, the presented data is averaged over an hour, showcasing the stability of the sample at fixed gate voltage on that timescale.

After having calibrated the length of our π pulse with the previously shown Rabi measurements, we move to Z rotations. In Fig. 3b, we employ virtual Z gates [53], involving two $\pi/2$ half pulses with an offset in the second pulse phase, introducing an artificial detuning (Δ). This approach mitigates the limited visibility and unwanted AC Stark shift when using a detuned pulse. We obtain a Ramsey pattern by sweeping the virtual detuning and the idle between the two $\pi/2$ pulses.

T_1 and T_2^* measurements

Having calibrated the pulse sequences using previously conducted measurements, we proceed to characterize our qubit relaxation and coherence times. We determine the relaxation time T_1 by initializing the qubit in the $|1\rangle$ state and adjusting the waiting time τ before applying the readout pulse. The characteristic decay time of the measured response is T_1 , which is extracted by fitting the data with $A \exp(-\tau/T_1) + B$, as illustrated in Fig. 4a. Next, we measure the coherence time, T_2^* , using the same pulse sequence used in the Ramsey plot in Fig. 3b. We choose an artificial detuning greater than the decoherence rate to observe a sufficient number of oscillations. This allows us to reliably extract T_2^* from $A \exp(-\tau/T_2^*) \cos(2\pi f\tau + \phi) + B + C\tau$, as depicted in

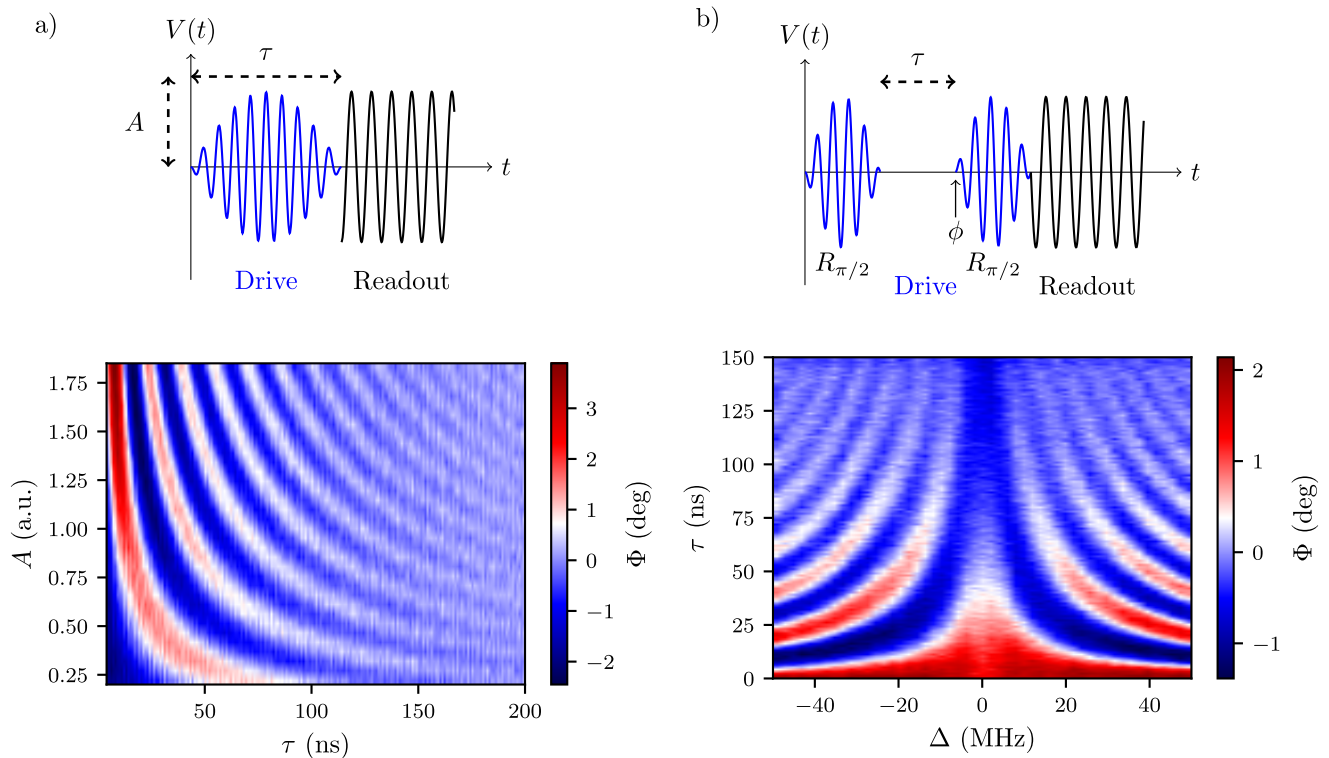


FIG. 3. Coherent control of the gatemon. a) Rabi oscillations at $f_q \approx 3.66$ GHz. We apply a cosine-shaped drive pulse directly on the gate line, followed by a readout pulse on the resonator line. b) Ramsey fringes with virtual Z gates. We rotate the frame of reference to mimic an extra rotation. The detuning defines the angle of rotation: $\phi = \Delta \cdot \tau$. In both a) and b), the measured response is averaged over 50000 traces, and the average of each column has been subtracted to account for the slow drift of the readout resonator.

Fig. 4b). Following this, we replicate the abovementioned procedures across multiple gate voltages, including qubit spectroscopy, Rabi, and Ramsey measurements. The results are presented in panels c) and d) of Fig. 4, where we display the extracted relaxation and coherence times as functions of the qubit frequency. The analysis yields a maximum T_1 of ≈ 73 ns across the scanned gate voltage range at $f_q \approx 2.8$ GHz. Additionally, we obtain a maximum T_2^* of 71 ns within the explored gate voltage range.

AL TRANSMON ON SIGE SUBSTRATE

To gain deeper insights, we compare our device with a fixed-frequency reference transmon measured on a similar substrate and in the same setup, see Fig. 5a. This transmon shares identical capacitor geometry, and its junction size (~ 200 nm X 180 nm) falls within the same range as the gatemon device presented (~ 400 nm X 150 nm). The choice of a fixed-frequency transmon aims to minimize losses in relaxation channels other than dielectric losses in the substrate. Notably, the hole gas is removed on the entire chip, and the junction is of a con-

ventional SIS type, with Al as superconductor (S) and AlO_x as an insulator (I). We determine the qubit frequency and extract T_1 and T_2^* times using techniques explained before. The measurements are detailed in Fig. 5 b,c, and d. We find $T_1 \approx 109$ ns and $T_2^* \approx 196$ ns, very close to the upper limit of $2T_1$.

DISCUSSION

To elucidate the underlying loss mechanisms of our gatemon, we draw comparisons between our findings on the semiconductor transmon and analysis from bare resonators measured on the same substrate, as outlined in Ref. [39]. We then complement the discussion by including the Al transmon figures in the comparison (Fig. 5). We start by converting the measured relaxation times into quality factors by using the expression $T_1 = Q/(2\pi f_q)$ [54]. In Fig. 4c, we fit the obtained relaxation times of the gatemon with this equation, which yields an "average" quality factor nearly five times lower than that measured with bare resonators on the same substrates [39]. This suggests additional losses beyond those originating from the substrate. This conclusion is

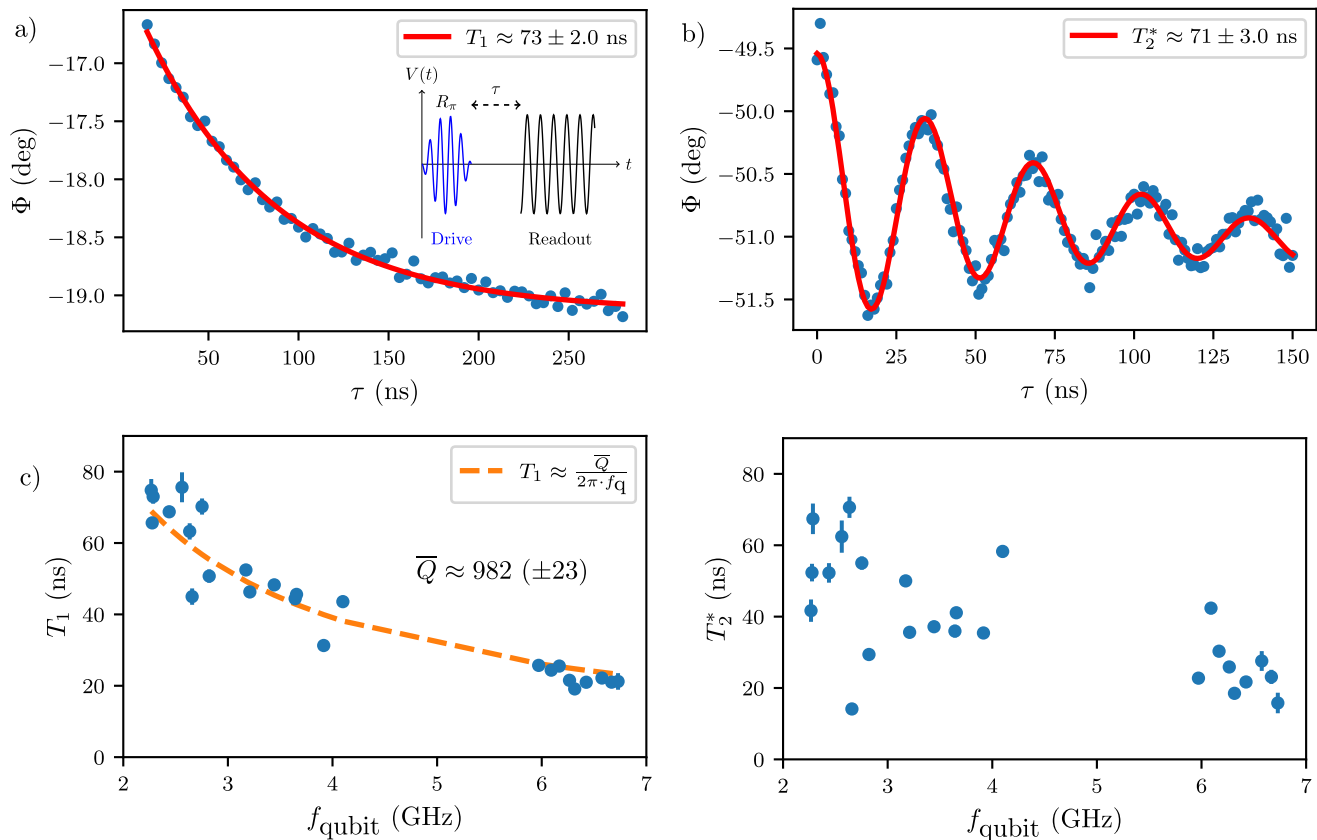


FIG. 4. Relaxation and coherence time measurements. a) T_1 measurement at $f_q \approx 2.8$ GHz. A 10 ns π pulse brings the qubit to the excited state, followed by a certain waiting time and the readout pulse. The solid red line is a fit to the exponential curve. b) T_2^* measurement at $f_q \approx 2.8$ GHz. The pulse sequence is identical to the one in Fig. 3b. The solid curve fits a damped sinusoidal curve on a linear background. The error bars represent the standard deviations of the fit. c) Relaxation time measurements as a function of qubit frequency. The error bars represent the standard deviations of the fit, depicted above. The dashed line indicates a fit to the function shown in the legend. We extract an effective quality factor lower than the Q_{is} of bare resonators on a similar substrate. d) Coherence time as a function of qubit frequency. The measured coherence times do not reach the $2T_1$ limit.

further supported by the fact that the Al transmon T_1 is approximately five times higher than in the semiconductor device at the same qubit frequency. We then delve into the disparities between the semiconductor gatemon and the Al transmon/resonators to shed light on the potential loss channels.

The first significant distinction is the gatemon mesa structure, which features a conducting two-dimensional hole gas covered with Al. Though a conductive layer normally would cause extra dissipation, Ref. [39] demonstrated that proximitized germanium (highlighted in red in Fig. 1b) does not introduce significant additional losses. Resonators defined atop proximitized germanium showed comparable internal quality factors (within a factor of two) to those defined with the quantum well etched away. Therefore, the presence of proximitized germanium alone cannot solely account for the reduced energy relaxation time.

The gatemon differs notably from both the SIS trans-

mon and bare resonators due to the presence of the Pd gate, which may introduce dissipative losses in the gatemon architecture due to its normal metal properties [55]. On top, the gate itself functions as a coplanar waveguide transmission line, adding another relaxation channel, but we rule out relaxation to the gate line or resonator as a limiting factor (refer to the Supplementary for further details). Moreover, Atomic Layer Deposition grown AlO_x is deposited across the entire gatemon device, including the qubit capacitor area where the electric field is concentrated, which can lead to additional dielectric losses [45]. It is also worth mentioning that semiconductor junctions may exhibit subgap states, potentially leading to quasi-particle losses due to external radiation [49, 56]. Finally, the analysis of coherence times of Fig. 4d reveals a non-monotonic trend, diverging from the $2T_1$ limit. This observation indicates that the coherence of the qubit is not fully constrained by energy relaxation but also influenced by dephasing attributed to charge fluctuators within the

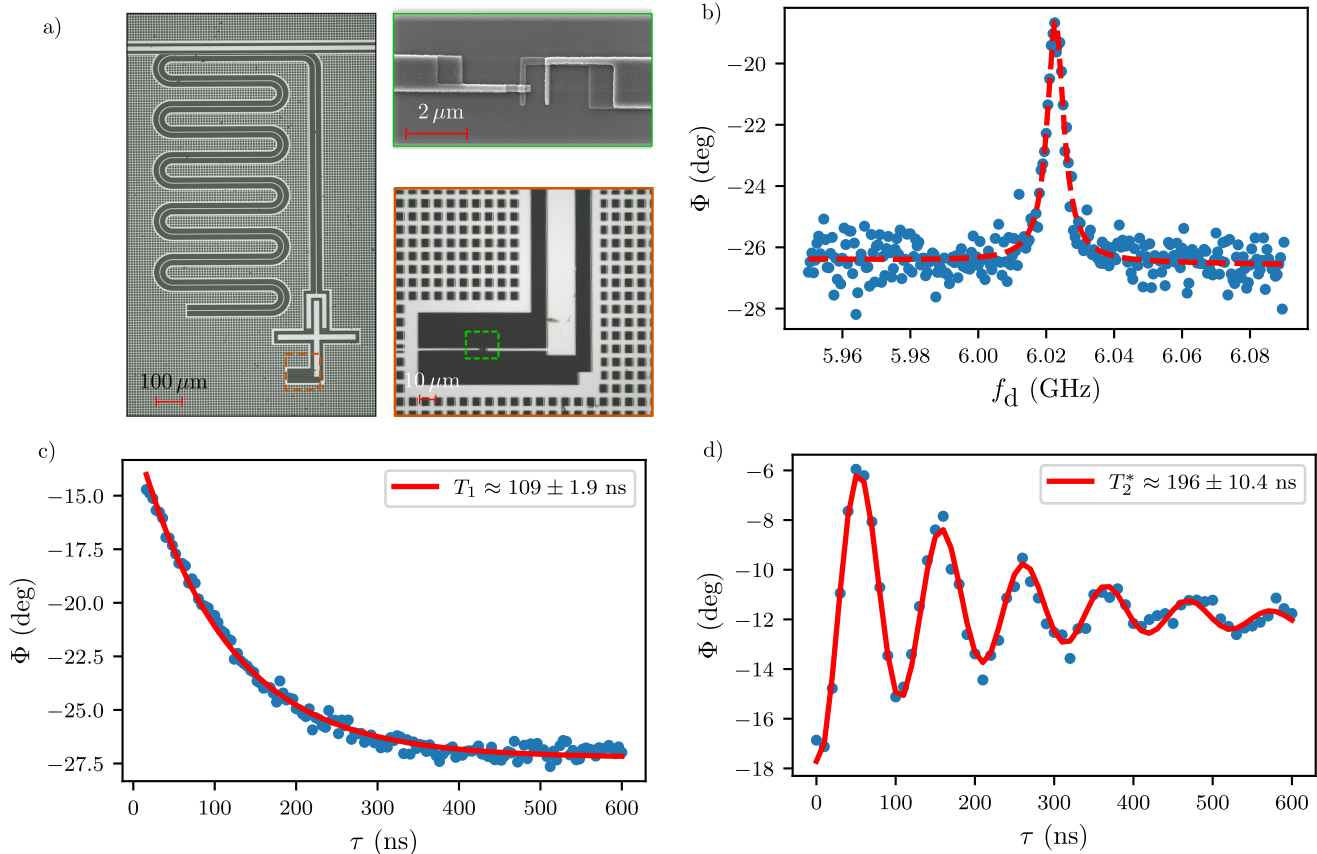


FIG. 5. Al transmon characterization on etched SiGe substrate. a) Overview of the device. We replaced the semiconductor junction with a shadow-evaporated Al-AlO_x-Al junction. Otherwise, we kept the device geometry the same. b) Qubit characterization with pulsed two-tone spectroscopy. The red dashed line represents a fit to a Lorentzian function. We choose the measurement frequency such that all information is contained in the phase of the measured signal. c). Relaxation time measurement using the same pulse sequence shown in Fig. 4. The solid red line is a fit to an exponential decay. d) Coherence time measurement using the same pulse sequence as shown in Fig. 4. The solid red line is a fit to a decaying sinusoidal oscillation.

oxide (covering the entire chip) [5].

SUMMARY

In summary, we have demonstrated a gate-tunable superconductor-semiconductor qubit on planar Ge. Our qubit shows broadband tunability and quasi-linear frequency dispersion, rendering it a promising element for ASQs and superconducting circuits requiring tunable elements. We have characterized the energy relaxation and coherence times, pinpointing the possible limitations with identified areas for improvement. One natural upgrade is to replace the Ti/Pd with either Al, Nb, or Ta, as exemplified in Ref. [55]. Losses in the oxide can be mitigated by lifting or etching the oxide with an additional fabrication step or switching to a low-loss dielectric, e.g., hBN [57]. To prolong the lifetimes of our gatemons beyond the constraints imposed by

dielectric losses in the buffer, one can explore strategies such as deep reactive ion etching [58] and flip-chip technology [20, 59].

With germanium already having solidified its position as a prominent player in the spin qubit domain [36, 60, 61], it is naturally considered an alternative platform for ASQs since current experiments are limited by dephasing due to nuclear spins [15]. To compete with III-V systems in ASQ platforms, the potential of Ge still needs to be demonstrated in the field of superconducting qubits. In that context, our work constitutes the entry of planar Ge in the field of hybrid qubits. Integrating gatemons in ASQ circuits will loosen up readout requirements by allowing in-situ frequency tuning and capacitive coupling to resonators [62]. Future challenges will involve addressing issues introduced by the shallow quantum wells [39] and improving the microwave properties of the substrates [63].

METHODS

Sample fabrication

First, we define the mesa structure with a depth of ~ 60 nm by etching away the hole gas with an $\text{SF}_6\text{-O}_2\text{-CHF}_3$ reactive ion etching process. The hole gas is etched away everywhere, except the mesa area, to remove the conducting hole gas below the microwave circuit. The Josephson junctions (JJs) are formed by evaporating at room temperature 80 nm Al on the mesa after a 15 s buffered HF dip. The Al is oxidized for 2 min at 10 mbar pressure before venting the evaporation chamber. The microwave circuitry is defined simultaneously with the JJ to reduce the number of fabrication steps. Finally, a plasma-assisted aluminum oxide, approximately 15 nm thick, is deposited at 150 °C, followed by the evaporation of Ti/Pd gates, where Ti was used as an adhesion layer. The thickness of the Al and Pd were chosen to be 20 nm greater than the mesa depth to ensure proper climbing of the edge.

Measurements

We performed all measurements in a cryogen-free dilution refrigerator with a base temperature below 10 mK. The sample was mounted on a custom printed circuit board thermally anchored to the mixing chamber of the cryostat, and electrical connections were made via wire bonding. The schematic of our measurement setup is shown in Fig. 13.

ACKNOWLEDGEMENTS

We acknowledge Lucas Casparis, Jeroen Danon, Valla Fatemi, Morten Kjaergard and Javad Shabani for their valuable insights and comments. This research was supported by the Scientific Service Units of ISTA through resources provided by the MIBA Machine Shop and the Nanofabrication facility. This research and related results were made possible with the support of the NOMIS Foundation and the FWF Projects with DOI:10.55776/I5060 and DOI:10.55776/P36507. We also acknowledge the NextGenerationEU PRIN project 2022A8CJP3 (GAMESQUAD) for partial financial support.

AUTHOR CONTRIBUTION

O.S. and L.B. were responsible for fabricating the devices, with O.S. conducting measurements and analyzing the data under the guidance of G.K. M.V. and O.S. collaborated on developing the nanofabrication recipe for

hybrid devices, while M.J. and O.S. were involved in developing the microwave technology for the Ge/SiGe heterostructures. G.F. contributed to device fabrication and measurements. S.C., D.C., and G.I. were responsible for the growth of the Ge QW. F.H. and L.K. provided assistance during the experiments. F.H., L.K., and J.F. provided the transmon nanofabrication recipe. O.S., A.C., and G.K. discussed the results and wrote the manuscript with contributions and feedback from all co-authors.

-
- * oliver.sagi@ista.ac.at
- [1] Z.-L. Xiang, S. Ashhab, J. Q. You, and F. Nori, Hybrid quantum circuits: Superconducting circuits interacting with other quantum systems, *Rev. Mod. Phys.* **85**, 623 (2013).
 - [2] R. Aguado, A perspective on semiconductor-based superconducting qubits, *Applied Physics Letters* **117**, 240501 (2020).
 - [3] G. De Lange, B. Van Heck, A. Bruno, D. Van Woerkom, A. Geresdi, S. Plissard, E. Bakkers, A. Akhmerov, and L. DiCarlo, Realization of microwave quantum circuits using hybrid superconducting-semiconducting nanowire josephson elements, *Physical review letters* **115**, 127002 (2015).
 - [4] T. W. Larsen, K. D. Petersson, F. Kuemmeth, T. S. Jespersen, P. Krogstrup, J. Nygård, and C. M. Marcus, Semiconductor-nanowire-based superconducting qubit, *Phys. Rev. Lett.* **115**, 127001 (2015).
 - [5] L. Casparis, M. R. Connolly, M. Kjaergaard, N. J. Pearson, A. Kringhøj, T. W. Larsen, F. Kuemmeth, T. Wang, C. Thomas, S. Gronin, G. C. Gardner, M. J. Manfra, C. M. Marcus, and K. D. Petersson, Superconducting gatemon qubit based on a proximitized two-dimensional electron gas, *Nature Nanotechnology* **13**, 915 (2018).
 - [6] T. W. Larsen, M. E. Gershenson, L. Casparis, A. Kringhøj, N. J. Pearson, R. P. G. McNeil, F. Kuemmeth, P. Krogstrup, K. D. Petersson, and C. M. Marcus, Parity-protected superconductor-semiconductor qubit, *Phys. Rev. Lett.* **125**, 056801 (2020).
 - [7] M. Hays, V. Fatemi, D. Bouman, J. Cerrillo, S. Diamond, K. Serniak, T. Connolly, P. Krogstrup, J. Nygård, A. L. Yeyati, A. Geresdi, and M. H. Devoret, Coherent manipulation of an andreev spin qubit, *Science* **373**, 430 (2021).
 - [8] M. Pita-Vidal, A. Bargerbos, R. Žitko, L. J. Splitthoff, L. Grünhaupt, J. J. Wesdorp, Y. Liu, L. P. Kouwenhoven, R. Aguado, B. van Heck, A. Kou, and C. K. Andersen, Direct manipulation of a superconducting spin qubit strongly coupled to a transmon qubit, *Nature Physics* **19**, 1110 (2023).
 - [9] J. I.-J. Wang, D. Rodan-Legrain, L. Bretheau, D. L. Campbell, B. Kannan, D. Kim, M. Kjaergaard, P. Krantz, G. O. Samach, F. Yan, J. L. Yoder, K. Watanabe, T. Taniguchi, T. P. Orlando, S. Gustavsson, P. Jarillo-Herrero, and W. D. Oliver, Coherent control of a hybrid superconducting circuit made with graphene-based van der waals heterostructures, *Nature Nanotechnology* **14**, 120 (2019).
 - [10] K.-L. Chiu, D. Qian, J. Qiu, W. Liu, D. Tan, V. Mosallanejad, S. Liu, Z. Zhang, Y. Zhao, and D. Yu, Flux tunable superconducting quantum circuit based on weyl semimetal mote2, *Nano Letters* **20**, 8469 (2020).
 - [11] M. Mergenthaler, A. Nersisyan, A. Patterson, M. Esposito, A. Baumgartner, C. Schönenberger, G. A. D. Briggs, E. A. Laird, and P. J. Leek, Circuit quantum electrodynamics with carbon-nanotube-based superconducting quantum circuits, *Phys. Rev. Appl.* **15**, 064050 (2021).
 - [12] T. W. Schmitt, M. R. Connolly, M. Schleenvoigt, C. Liu, O. Kennedy, J. M. Chávez-García, A. R. Jalil, B. Benne- mann, S. Trellenkamp, F. Lentz, E. Neumann, T. Lindström, S. E. de Graaf, E. Berenschot, N. Tas, G. Mussler, K. D. Petersson, D. Grützmacher, and P. Schüffelgen, Integration of topological insulator josephson junctions in superconducting qubit circuits, *Nano Letters* **22**, 2595 (2022).
 - [13] A. Blais, A. L. Grimsmo, S. M. Girvin, and A. Wallraff, Circuit quantum electrodynamics, *Rev. Mod. Phys.* **93**, 025005 (2021).
 - [14] L. Y. Cheung, R. Haller, A. Kononov, C. Ciaccia, J. H. Ungerer, T. Kanne, J. Nygård, P. Winkel, T. Reisinger, I. M. Pop, A. Baumgartner, and C. Schönenberger, Photon-mediated long range coupling of two andreev level qubits (2023), arXiv:2310.15995 [cond-mat.mes-hall].
 - [15] M. Pita-Vidal, J. J. Wesdorp, L. J. Splitthoff, A. Bargerbos, Y. Liu, L. P. Kouwenhoven, and C. K. Andersen, Strong tunable coupling between two distant superconducting spin qubits (2023), arXiv:2307.15654 [quant-ph].
 - [16] M. Spethmann, X.-P. Zhang, J. Klinovaja, and D. Loss, Coupled superconducting spin qubits with spin-orbit interaction, *Phys. Rev. B* **106**, 115411 (2022).
 - [17] J. Dijkema, X. Xue, P. Harvey-Collard, M. Rimbach-Russ, S. L. de Snoo, G. Zheng, A. Sammak, G. Scappucci, and L. M. K. Vandersypen, Two-qubit logic between distant spins in silicon (2023), arXiv:2310.16805 [cond-mat.mes-hall].
 - [18] F. Borjans, X. G. Croot, X. Mi, M. J. Gullans, and J. R. Petta, Resonant microwave-mediated interactions between distant electron spins, *Nature* **577**, 195 (2020).
 - [19] P. Harvey-Collard, J. Dijkema, G. Zheng, A. Sammak, G. Scappucci, and L. M. K. Vandersypen, Coherent spin-spin coupling mediated by virtual microwave photons, *Phys. Rev. X* **12**, 021026 (2022).
 - [20] M. Hinderling, S. C. ten Kate, M. Coraiola, D. Z. Haxell, M. Stiefel, M. Mergenthaler, S. Paredes, S. W. Bedell, D. Sabonis, and F. Nichele, Direct microwave spectroscopy of andreev bound states in planar ge josephson junctions (2024), arXiv:2403.03800 [cond-mat.mes-hall].
 - [21] M. Vinet, L. Hutin, B. Bertrand, S. Barraud, J.-M. Hartmann, Y.-J. Kim, V. Mazzocchi, A. Amisse, H. Bohuslavskiy, L. Bourdet, A. Crippa, X. Jehl, R. Maurand, Y.-M. Niquet, M. Sanquer, B. Venitucci, B. Jadot, E. Chanrion, P.-A. Mortemousque, C. Spence, M. Urdampilleta, S. De Franceschi, and T. Meunier, Towards scalable silicon quantum computing, in *International Electron Devices Meeting (IEDM) (IEEE, 2018)* pp. 6.5.1–6.5.4.
 - [22] G. Burkard, T. D. Ladd, A. Pan, J. M. Nichol, and J. R. Petta, Semiconductor spin qubits, *Rev. Mod. Phys.* **95**, 025003 (2023).
 - [23] X. Mi, M. Benito, S. Putz, D. M. Zajac, J. M. Taylor, G. Burkard, and J. R. Petta, A coherent spin-photon interface in silicon, *Nature* **555**, 599 (2018).
 - [24] C. X. Yu, S. Zihlmann, J. C. Abadillo-Uriel, V. P. Michal, N. Rambal, H. Niebojewski, T. Bedecarrats, M. Vinet, É. Dumur, M. Filippone, B. Bertrand, S. De Franceschi, Y.-M. Niquet, and R. Maurand, Strong coupling between a photon and a hole spin in silicon, *Nature Nanotechnology* **18**, 741 (2023).
 - [25] N. Samkharadze, G. Zheng, N. Kalhor, D. Brousse, A. Sammak, U. C. Mendes, A. Blais, G. Scappucci, and L. M. K. Vandersypen, Strong spin-photon coupling in silicon, *Science* **359**, 1123 (2018).
 - [26] E. Bustarret, C. Marcenat, P. Achatz, J. Kačmarčík, F. Lévy, A. Huxley, L. Ortéga, E. Bourgeois, X. Blase,

- D. Débarre, and J. Boulmer, Superconductivity in doped cubic silicon, *Nature* **444**, 465 (2006).
- [27] T. D. Vethaak, Silicide-based josephson field effect transistors for superconducting qubits (2022), arXiv:2209.02721 [physics.app-ph].
- [28] J. Shabani, M. Kjaergaard, H. J. Suominen, Y. Kim, F. Nichele, K. Pakrouski, T. Stankevic, R. M. Lutchyn, P. Krogstrup, R. Feidenhans'l, S. Kraemer, C. Nayak, M. Troyer, C. M. Marcus, and C. J. Palmstrøm, Two-dimensional epitaxial superconductor-semiconductor heterostructures: A platform for topological superconducting networks, *Phys. Rev. B* **93**, 155402 (2016).
- [29] P. Krogstrup, N. L. B. Ziino, W. Chang, S. M. Albrecht, M. H. Madsen, E. Johnson, J. Nygård, C. M. Marcus, and T. S. Jespersen, Epitaxy of semiconductor–superconductor nanowires, *Nature Materials* **14**, 400 (2015).
- [30] M. Kjaergaard, H. J. Suominen, M. P. Nowak, A. R. Akhmerov, J. Shabani, C. J. Palmstrøm, F. Nichele, and C. M. Marcus, Transparent semiconductor–superconductor interface and induced gap in an epitaxial heterostructure josephson junction, *Phys. Rev. Appl.* **7**, 034029 (2017).
- [31] R. M. Lutchyn, E. P. A. M. Bakkers, L. P. Kouwenhoven, P. Krogstrup, C. M. Marcus, and Y. Oreg, Majorana zero modes in superconductor–semiconductor heterostructures, *Nature Reviews Materials* **3**, 52 (2018).
- [32] S. Nadj-Perge, S. M. Frolov, E. P. A. M. Bakkers, and L. P. Kouwenhoven, Spin–orbit qubit in a semiconductor nanowire, *Nature* **468**, 1084 (2010).
- [33] N. W. Hendrickx, D. P. Franke, A. Sammak, M. Kouwenhoven, D. Sabbagh, L. Yeoh, R. Li, M. L. V. Tagliaferri, M. Virgilio, G. Capellini, G. Scappucci, and M. Veldhorst, Gate-controlled quantum dots and superconductivity in planar germanium, *Nature Communications* **9**, 2835 (2018).
- [34] D. Jirovec, A. Hofmann, A. Ballabio, P. M. Mutter, G. Tavani, M. Botifoll, A. Crippa, J. Kukucka, O. Sagi, F. Martins, J. Saez-Mollejo, I. Prieto, M. Borovkov, J. Arbiol, D. Chrastina, G. Isella, and G. Katsaros, A singlet-triplet hole spin qubit in planar ge, *Nature Materials* **20**, 1106 (2021).
- [35] N. W. Hendrickx, L. Massai, M. Mergenthaler, F. Schupp, S. Paredes, S. W. Bedell, G. Salis, and A. Fuhrer, Sweet-spot operation of a germanium hole spin qubit with highly anisotropic noise sensitivity (2023), arXiv:2305.13150 [cond-mat.mes-hall].
- [36] C.-A. Wang, V. John, H. Tidjani, C. X. Yu, A. Ivlev, C. Déprez, F. van Riggelen-Doelman, B. D. Woods, N. W. Hendrickx, W. I. L. Lawrie, L. E. A. Stehouwer, S. Oosterhout, A. Sammak, M. Friesen, G. Scappucci, S. L. de Snoo, M. Rimbach-Russ, F. Borsoi, and M. Veldhorst, Operating semiconductor quantum processors with hopping spins (2024), arXiv:2402.18382 [cond-mat.mes-hall].
- [37] F. Vigneau, R. Mizokuchi, D. C. Zanuz, X. Huang, S. Tan, R. Maurand, S. Frolov, A. Sammak, G. Scappucci, F. Lefloch, and S. De Franceschi, Germanium quantum-well josephson field-effect transistors and interferometers, *Nano Letters* **19**, 1023 (2019).
- [38] K. Aggarwal, A. Hofmann, D. Jirovec, I. Prieto, A. Sammak, M. Botifoll, S. Martí-Sánchez, M. Veldhorst, J. Arbiol, G. Scappucci, J. Danon, and G. Katsaros, Enhancement of proximity-induced superconductivity in a planar ge hole gas, *Phys. Rev. Res.* **3**, L022005 (2021).
- [39] M. Valentini, O. Sagi, L. Baghumyan, T. de Gijssels, J. Jung, S. Calcaterra, A. Ballabio, J. Aguilera Servin, K. Aggarwal, M. Janik, T. Adletzberger, R. Seoane Souto, M. Leijnse, J. Danon, C. Schrade, E. Bakkers, D. Chrastina, G. Isella, and G. Katsaros, Parity-conserving cooper-pair transport and ideal superconducting diode in planar germanium, *Nature Communications* **15**, 169 (2024).
- [40] G. Scappucci, C. Kloeffer, F. A. Zwanenburg, D. Loss, M. Myronov, J.-J. Zhang, S. De Franceschi, G. Katsaros, and M. Veldhorst, The germanium quantum information route, *Nature Reviews Materials* **6**, 926 (2021).
- [41] E. Zhuo, Z. Lyu, X. Sun, A. Li, B. Li, Z. Ji, J. Fan, E. P. A. M. Bakkers, X. Han, X. Song, F. Qu, G. Liu, J. Shen, and L. Lu, Hole-type superconducting gatemon qubit based on ge/si core/shell nanowires, *npj Quantum Information* **9**, 51 (2023).
- [42] H. Zheng, L. Y. Cheung, N. Sangwan, A. Kononov, R. Haller, J. Ridderbos, C. Ciaccia, J. H. Ungerer, A. Li, E. P. A. M. Bakkers, A. Baumgartner, and C. Schönenberger, Coherent control of a few-channel hole type gatemon qubit (2023), arXiv:2312.06411 [cond-mat.mes-hall].
- [43] M. J. Carballido, S. Svab, R. S. Egli, T. Patlatiuk, P. C. Kwon, J. Schuff, R. M. Kaiser, L. C. Camenzind, A. Li, N. Ares, E. P. A. M. Bakkers, S. Bosco, J. C. Egues, D. Loss, and D. M. Zumbühl, A qubit with simultaneously maximized speed and coherence (2024), arXiv:2402.07313 [cond-mat.mes-hall].
- [44] F. N. M. Froning, L. C. Camenzind, O. A. H. van der Molen, A. Li, E. P. A. M. Bakkers, D. M. Zumbühl, and F. R. Braakman, Ultrafast hole spin qubit with gate-tunable spin–orbit switch functionality, *Nature Nanotechnology* **16**, 308 (2021).
- [45] W. M. Strickland, J. Lee, L. Baker, K. Dindial, B. H. Elfeky, M. Hatefipour, P. Yu, I. Levy, V. E. Manucharyan, and J. Shabani, Characterizing losses in inas two-dimensional electron gas-based gatemon qubits (2023), arXiv:2309.17273 [quant-ph].
- [46] R. Barends, J. Kelly, A. Megrant, D. Sank, E. Jeffrey, Y. Chen, Y. Yin, B. Chiaro, J. Mutus, C. Neill, P. O'Malley, P. Roushan, J. Wenner, T. C. White, A. N. Cleland, and J. M. Martinis, Coherent josephson qubit suitable for scalable quantum integrated circuits, *Phys. Rev. Lett.* **111**, 080502 (2013).
- [47] R. Barends, J. Kelly, A. Megrant, A. Veitia, D. Sank, E. Jeffrey, T. C. White, J. Mutus, A. G. Fowler, B. Campbell, Y. Chen, Z. Chen, B. Chiaro, A. Dunsworth, C. Neill, P. O'Malley, P. Roushan, A. Vainsencher, J. Wenner, A. N. Korotkov, A. N. Cleland, and J. M. Martinis, Superconducting quantum circuits at the surface code threshold for fault tolerance, *Nature* **508**, 500 (2014).
- [48] J. Koch, T. M. Yu, J. Gambetta, A. A. Houck, D. I. Schuster, J. Majer, A. Blais, M. H. Devoret, S. M. Girvin, and R. J. Schoelkopf, Charge-insensitive qubit design derived from the cooper pair box, *Phys. Rev. A* **76**, 042319 (2007).
- [49] A. Kringhøj, T. W. Larsen, O. Erlandsson, W. Uilhoorn, J. Kroll, M. Hesselberg, R. McNeil, P. Krogstrup, L. Casparis, C. Marcus, and K. Petersson, Magnetic-field-compatible superconducting transmon qubit, *Phys.*

- Rev. Appl. **15**, 054001 (2021).
- [50] F. Luthi, T. Stavenga, O. W. Enzing, A. Bruno, C. Dickel, N. K. Langford, M. A. Rol, T. S. Jespersen, J. Nygård, P. Krogstrup, and L. DiCarlo, Evolution of nanowire transmon qubits and their coherence in a magnetic field, *Phys. Rev. Lett.* **120**, 100502 (2018).
- [51] C. W. J. Beenakker, Universal limit of critical-current fluctuations in mesoscopic josephson junctions, *Phys. Rev. Lett.* **67**, 3836 (1991).
- [52] A. Kringhøj, L. Casparis, M. Hell, T. W. Larsen, F. Kuemmeth, M. Leijnse, K. Flensberg, P. Krogstrup, J. Nygård, K. D. Petersson, and C. M. Marcus, Anharmonicity of a superconducting qubit with a few-mode josephson junction, *Phys. Rev. B* **97**, 060508 (2018).
- [53] D. C. McKay, C. J. Wood, S. Sheldon, J. M. Chow, and J. M. Gambetta, Efficient z gates for quantum computing, *Phys. Rev. A* **96**, 022330 (2017).
- [54] C. R. H. McRae, H. Wang, J. Gao, M. R. Vissers, T. Brecht, A. Dunsworth, D. P. Pappas, and J. Mutus, Materials loss measurements using superconducting microwave resonators, *Review of Scientific Instruments* **91**, 091101 (2020).
- [55] W. M. Strickland, B. H. Elfeky, J. O. Yuan, W. F. Schiela, P. Yu, D. Langone, M. G. Vavilov, V. E. Manucharyan, and J. Shabani, Superconducting resonators with voltage-controlled frequency and nonlinearity, *Phys. Rev. Appl.* **19**, 034021 (2023).
- [56] C. H. Liu, D. C. Harrison, S. Patel, C. D. Wilen, O. Raftery, A. Shearow, A. Ballard, V. Iaia, J. Ku, B. L. T. Plourde, and R. McDermott, Quasiparticle poisoning of superconducting qubits from resonant absorption of pair-breaking photons, *Phys. Rev. Lett.* **132**, 017001 (2024).
- [57] J. I.-J. Wang, M. A. Yamoah, Q. Li, A. H. Karamlou, T. Dinh, B. Kannan, J. Braumüller, D. Kim, A. J. Melville, S. E. Muschinske, B. M. Niedzielski, K. Serniak, Y. Sung, R. Winik, J. L. Yoder, M. E. Schwartz, K. Watanabe, T. Taniguchi, T. P. Orlando, S. Gustavsson, P. Jarillo-Herrero, and W. D. Oliver, Hexagonal boron nitride as a low-loss dielectric for superconducting quantum circuits and qubits, *Nature Materials* **21**, 398 (2022).
- [58] S. Probst, F. B. Song, P. A. Bushev, A. V. Ustinov, and M. Weides, Efficient and robust analysis of complex scattering data under noise in microwave resonators, *Review of Scientific Instruments* **86**, 024706 (2015).
- [59] T. Hazard, A. Kerman, K. Serniak, and C. Tahan, Superconducting-semiconducting voltage-tunable qubits in the third dimension, *Phys. Rev. Appl.* **20**, 034056 (2023).
- [60] F. Borsoi, N. W. Hendrickx, V. John, M. Meyer, S. Motz, F. van Riggelen, A. Sammak, S. L. de Snoo, G. Scappucci, and M. Veldhorst, Shared control of a 16 semiconductor quantum dot crossbar array, *Nature Nanotechnology* **19**, 21 (2024).
- [61] N. W. Hendrickx, W. I. L. Lawrie, M. Russ, F. van Riggelen, S. L. de Snoo, R. N. Schouten, A. Sammak, G. Scappucci, and M. Veldhorst, A four-qubit germanium quantum processor, *Nature* **591**, 580 (2021).
- [62] A. Bargerbos, M. Pita-Vidal, R. Žitko, J. Ávila, L. J. Splitthoff, L. Grünhaupt, J. J. Wesdorp, C. K. Andersen, Y. Liu, L. P. Kouwenhoven, R. Aguado, A. Kou, and B. van Heck, Singlet-doublet transitions of a quantum dot josephson junction detected in a transmon circuit, *PRX Quantum* **3**, 030311 (2022).
- [63] M. Sandberg, V. P. Adiga, M. Brink, C. Kurter, C. Murray, M. Hopstaken, J. Bruley, J. S. Orcutt, and H. Paik, Investigating microwave loss of SiGe using superconducting transmon qubits, *Applied Physics Letters* **118**, 124001 (2021).
- [64] A. A. Houck, J. A. Schreier, B. R. Johnson, J. M. Chow, J. Koch, J. M. Gambetta, D. I. Schuster, L. Frunzio, M. H. Devoret, S. M. Girvin, and R. J. Schoelkopf, Controlling the spontaneous emission of a superconducting transmon qubit, *Phys. Rev. Lett.* **101**, 080502 (2008).
- [65] S. Burkhard, Optimization of transmon design for longer coherence time (2012).

SUPPLEMENTARY DATA

Additional loss mechanisms

The measured T_1 times range from 75 to 20 ns. Here, we demonstrate that we are not limited by design constraints, i.e., decay to the resonator and the gate (drive) line. To estimate the Purcell limit, we extract the bare resonator properties as depicted in Fig. 6. The obtained Purcell limit at the smallest detuning reads [64]:

$T_{\text{Purcell}} = \left(\kappa (g/\Delta)^2 \right)^{-1} \approx 400 \text{ ns}$ ($\kappa \approx 2\pi \cdot 3.4 \text{ MHz}$ and $\max(g/\Delta) \approx 0.34$, $|\Delta_{\text{min}}| \approx 0.8 \text{ GHz}$). The calculated Purcell limit is an order of magnitude higher than the measured T_1 times. Thus, it is not a limiting factor. The same analysis holds for the reference transmons. The coupling strength is derived from a power-dependent resonator spectroscopy measurement, shown in Fig. 12. Our analysis yields a coupling strength of approximately $g/2\pi \approx 94 \text{ MHz}$, a detuning of approxi-

mately $|\Delta| \approx 1.26 \text{ GHz}$, and a linewidth of approximately $\kappa \approx 2.23 \cdot 2\pi \text{ MHz}$. These parameters result in a Purcell time (T_{Purcell}) of approximately $12 \mu\text{s}$, which is two orders of magnitude higher than the measured T_1 .

To estimate the relaxation to the drive line, we model the gatemon as an LC resonator capacitively coupled to the unfiltered $Z = 50 \Omega$ designed (impedance of the drive line) transmission line, acting as a gate. The environmental 50Ω impedance will dissipate the energy escaping the gatemon circuit. We estimate the T_1 limit following the formula in Refs. [48, 65]:

$$T_{\text{drive}} \approx \frac{4C}{RC_g^2\omega^2} \approx 22 \mu\text{s}, \quad (3)$$

where $Z_0 \approx 50 \Omega$ is the impedance of the feedline, $C \approx 85 \text{ fF}$ is the impedance of the gatemon circuit, $\omega \approx 2\pi \cdot 5 \text{ GHz}$ is the resonant frequency and $C_g \approx 0.57 \text{ fF}$ is the capacitance between the gatemon circuit and the feedline.

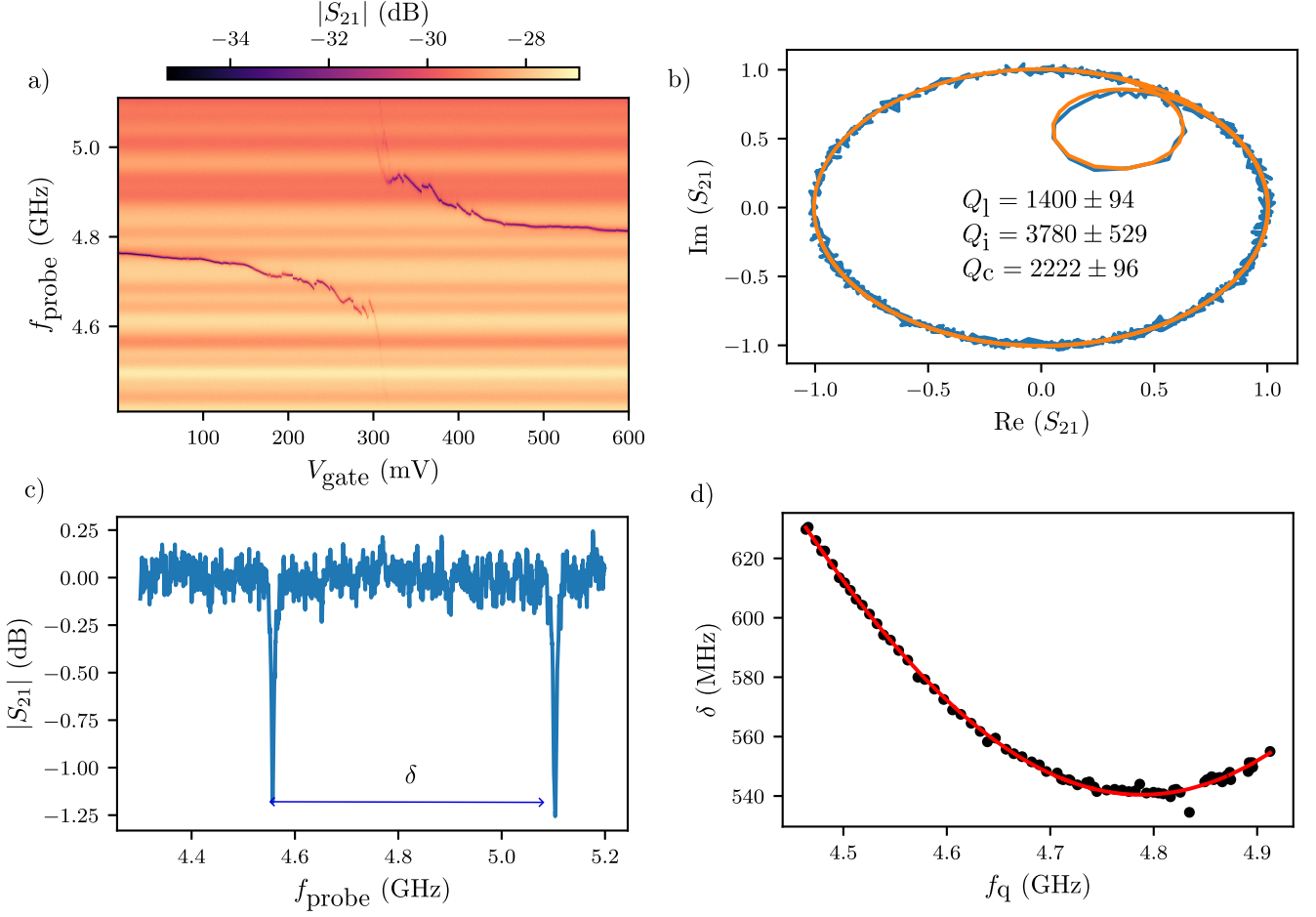


FIG. 6. Extended resonator spectroscopy data on the device presented in the main text. a) VNA sweep for a broader gate range without background correction at $n_{\text{ph}} \approx 1$ power level. b) Fit to extract the bare resonator properties taken at $V_{\text{g}} = 700$ mV where the qubit is very far detuned from the resonator. We fit the complex S_{21} parameter with the *resonator-tools* [58] package. c) Line-cut from Fig. 1e at $V_{\text{g}} = 307$ mV. We denote the splitting of the hybridized resonator-qubit states by δ as mentioned in the main text. d) Extracted splitting as a function of the qubit frequency. The solid red line is a fit according to Eq. 1 using g as a free parameter.

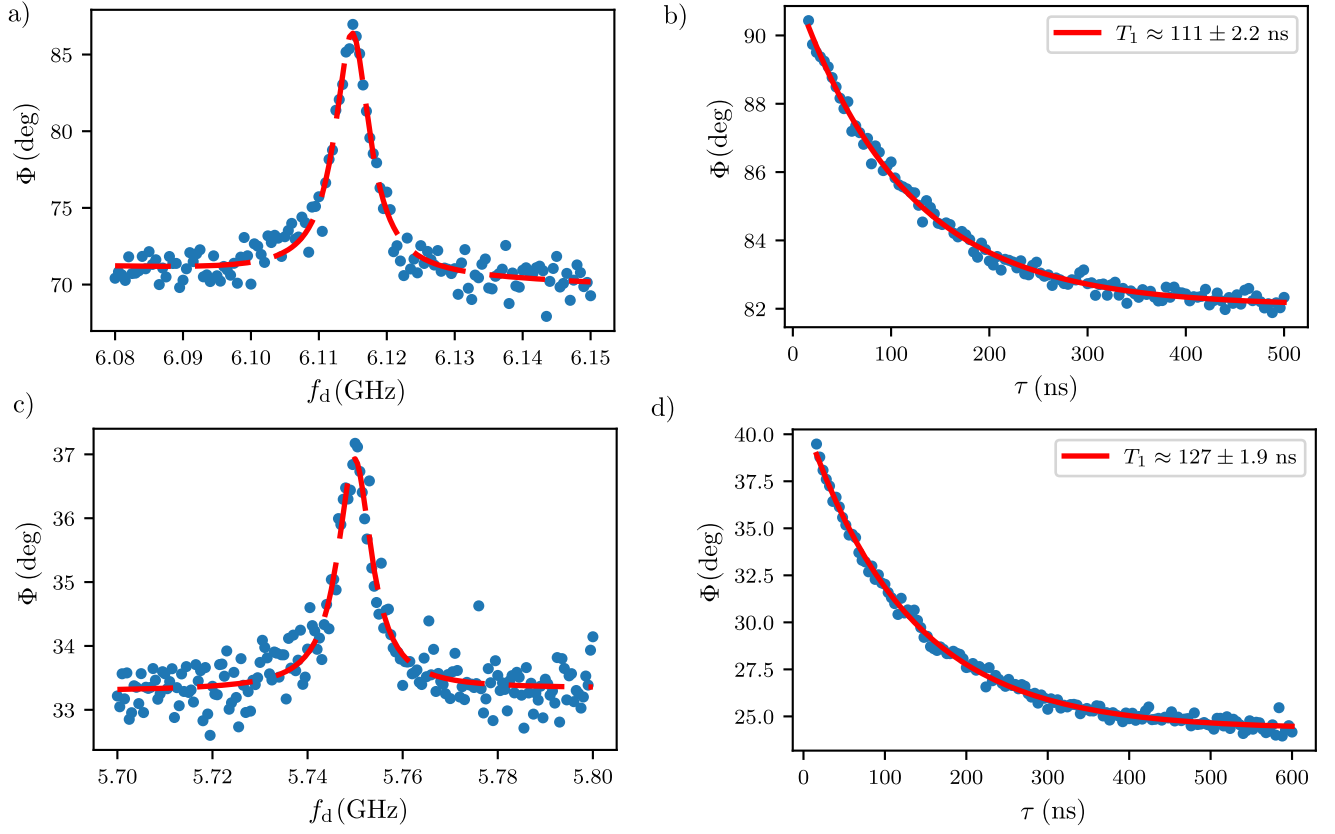


FIG. 7. Data from two additional Al transmons, one related to panels a) and b), the other to panels c) and d). The devices presented are identical to the one shown in Fig. 5, except for the junction size, which varies to get different qubit frequencies. a), c) Qubit spectroscopy with pulsed two-tone measurement. b), d) Energy relaxation measurements. The measured results are consistent with the ones presented in the main text.

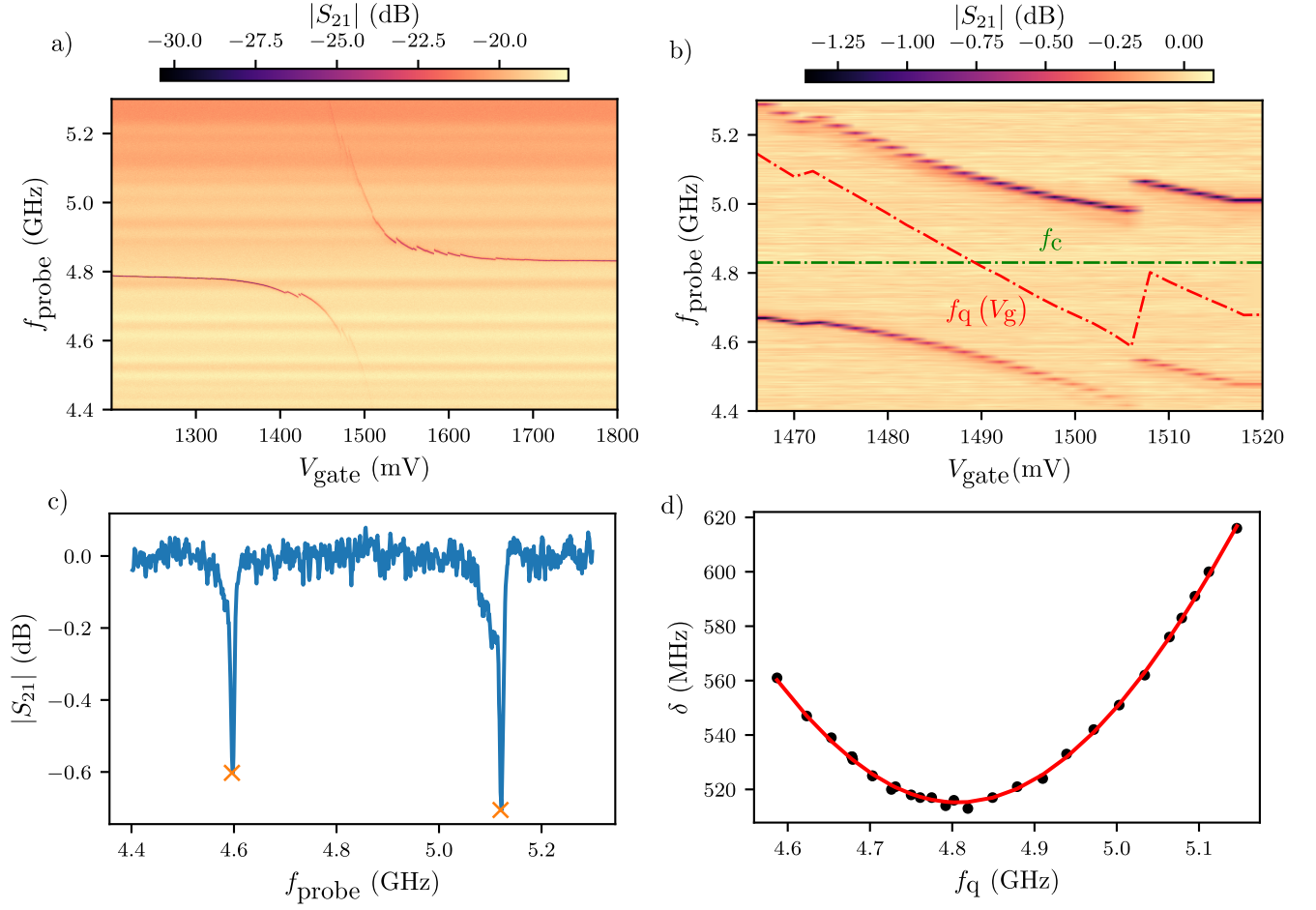


FIG. 8. Resonator spectroscopy on a second Ge gatemon device. Apart from the junction length, which is 50 nm shorter, the second device is nominally identical to the first one discussed in the main text. a) VNA sweep at low photon number. Since the junction is shorter compared to the sample of the main text, we needed to operate in a different gate voltage range to obtain the same critical current. b) Zoom-in of panel a). We observe two peaks due to qubit-resonator hybridization. c). One-dimensional line-cut at $V_g = 1494$ mV. d) Coupling strength extraction in the same way as demonstrated in Fig. 6. We extract a coupling value of $g/2\pi \approx 257$ MHz, consistent with g obtained in Fig. 6d.

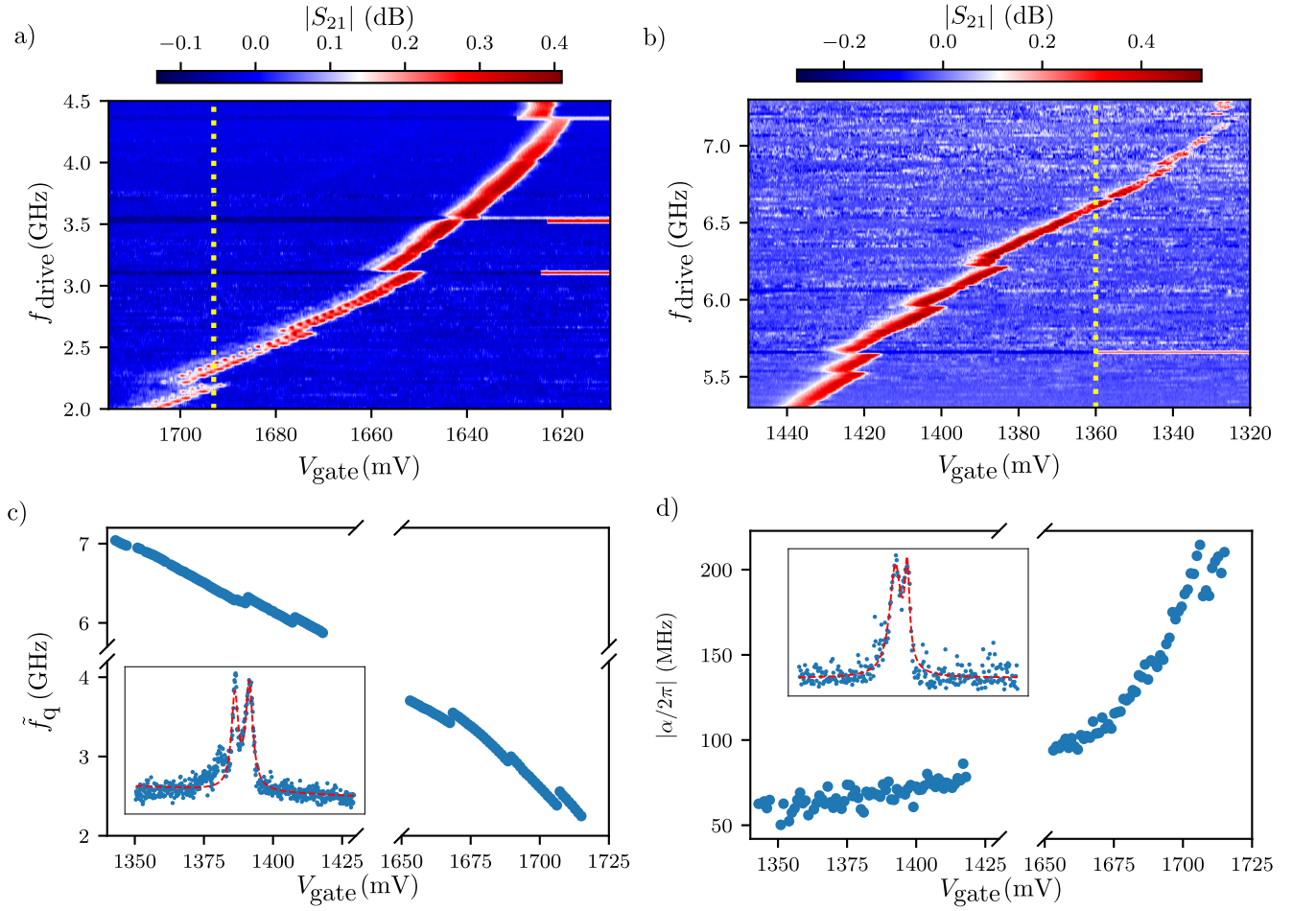


FIG. 9. Continuous-wave two-tone spectroscopy on a second gatemon device. The simplicity of continuous measurements allowed for quick characterization. a)-b) Raw two-tone spectroscopy data acquired with a VNA. We choose a high enough power to see the $|0\rangle \rightarrow |2\rangle$ transition via a two-photon process to obtain the anharmonicity with the same measurement. The qubit broadens due to photon shot noise as it moves closer to the resonator since the measurement and drive tone are applied simultaneously. We have subtracted the average of each column at every gate voltage. c) Extracted qubit frequencies versus gate voltage. The inset shows a linecut at $V_g = 1693$ mV indicated by the yellow dashed line in panel a). We fit each trace with a double Lorentzian curve. The center of the second peak yields the qubit frequency. d) Extracted anharmonicity versus gate voltage. The inset shows a linecut at $V_g = 1360$ mV indicated by the yellow dashed line in panel b). The distance between the peaks is the half of the anharmonicity.

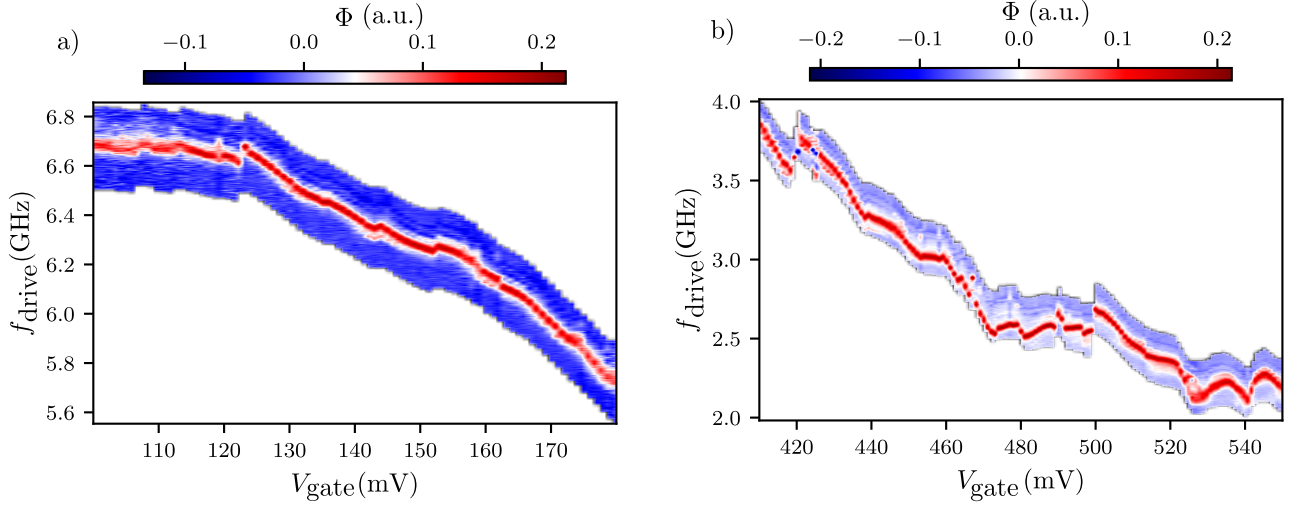


FIG. 10. Three-tone spectroscopy measurements used to extract the anharmonicity presented in Fig. 2d, with $f_q > f_r$ and $f_q < f_r$ shown in panel a) and b) respectively. The position of the measured peak yields the frequency of the $|1\rangle \rightarrow |2\rangle$ transition. At $V_g < 100$ mV, we observe two peaks in the two-tone spectroscopy measurement. Thus, we have left that region out in that measurement.

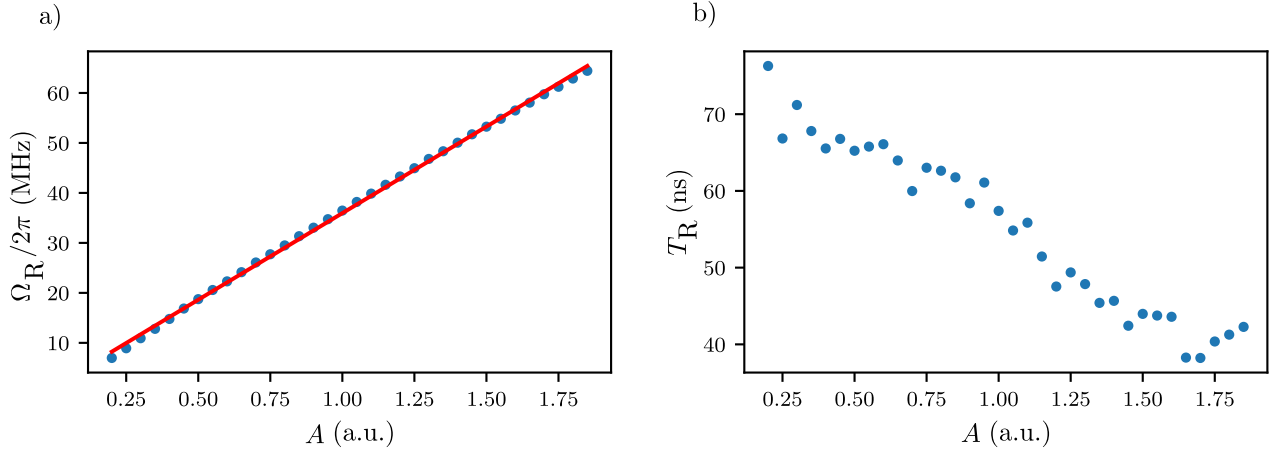


FIG. 11. Rabi frequency (panel a) and Rabi times (panel b) as a function of amplitude extracted from Fig. 3 from the main text. At each amplitude, we fitted the trace with the following expression: $A \cos(\Omega_R t + \varphi) \exp(-t/T_R) + B$.

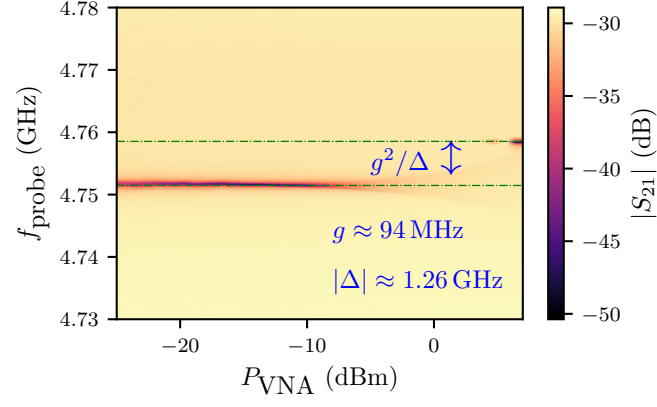


FIG. 12. Normalized feed line transmission of the reference transmon as a function of readout power. We observe a Lamb shift $\chi_0 = g^2/\Delta \approx 7$ MHz as a signature of coupling to a non-harmonic system. We extract the linewidth κ of the resonator at $P_{\text{VNA}} = -25$ dBm.

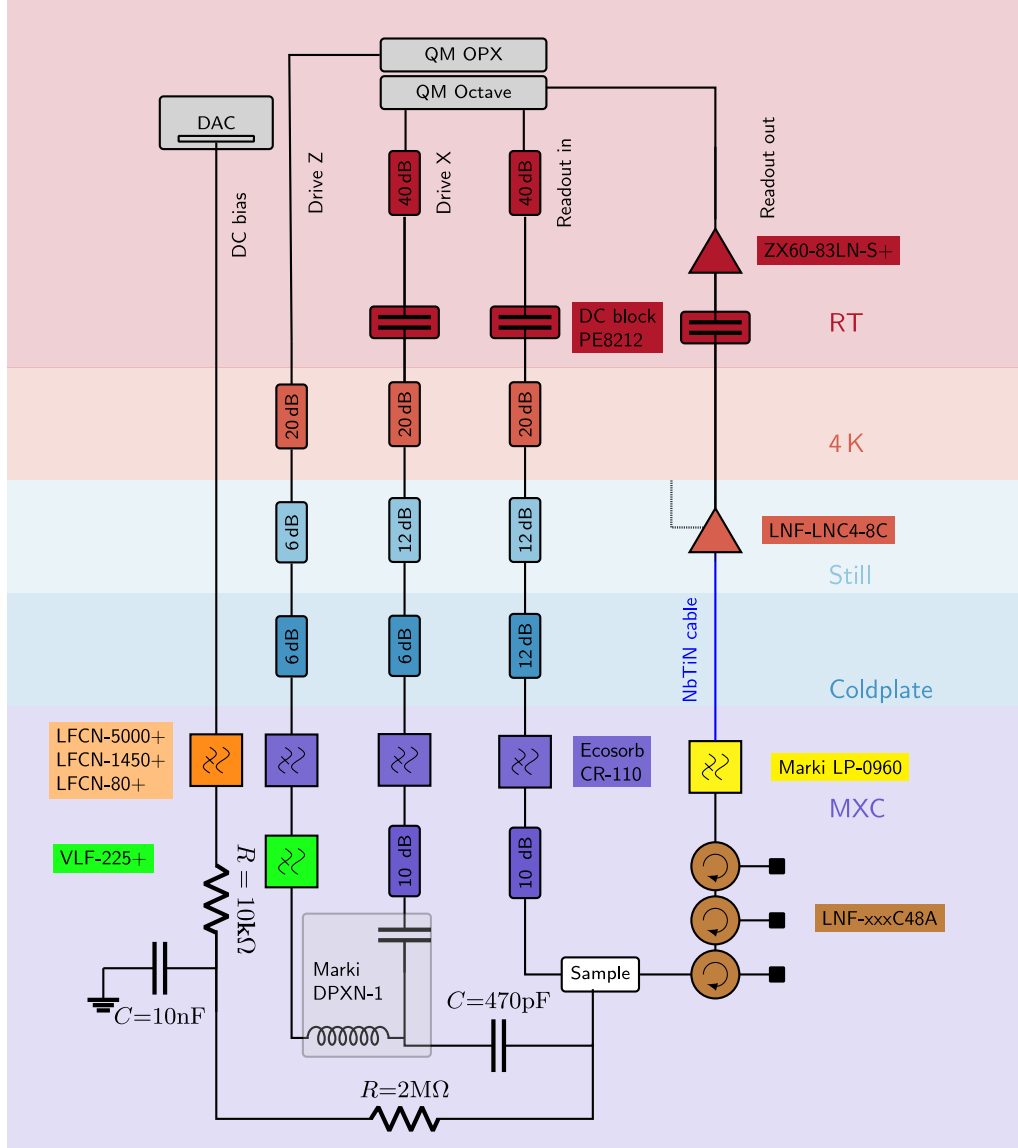


FIG. 13. Schematics of the fridge wiring and measurement setup. The *Readout in* and *Readout out* lines are connected to a VNA for continuous-wave measurements. For time-domain measurements, we have used Quantum Machines (QM) instruments. We have used *Drive X* line to send microwave (GHz) pulses, whereas the *Drive Z* line is intended for sending DC pulses. We combine the two lines at the MXC. The *Drive Z* line is not used in this experiment.